



Article

Investigation of Vacancy-Ordered Double Perovskite Halides $A_2Sn_{1-x}Ti_xY_6$ (A = K, Rb, Cs; Y = Cl, Br, I): Promising Materials for Photovoltaic Applications

Wen Chen ¹, Gang Liu ^{2,*}, Chao Dong ³, Xiaoning Guan ³, Shuli Gao ¹, Jinbo Hao ¹ , Changcheng Chen ^{1,*} and Pengfei Lu ³

¹ School of Science, Xi'an University of Architecture and Technology, Xi'an 710055, China; chenwen@xauat.edu.cn (W.C.); gaoshuli@xauat.edu.cn (S.G.); jbhao@xauat.edu.cn (J.H.)

² School of Electronic Engineering, Beijing University of Posts and Telecommunications, Beijing 100876, China

³ School of Integrated Circuits, Beijing University of Posts and Telecommunications, Beijing 100876, China; chaodong@bupt.edu.cn (C.D.); guanxn@bupt.edu.cn (X.G.); lupengfei@bupt.edu.cn (P.L.)

* Correspondence: liu_gang@bupt.edu.cn (G.L.); chenchangcheng@xauat.edu.cn (C.C.)

Abstract: In the present study, the structural, mechanical, electronic and optical properties of all-inorganic vacancy-ordered double perovskites $A_2Sn_{1-x}Ti_xY_6$ (A = K, Rb, Cs; Y = Cl, Br, I) are explored by density functional theory. The structural and thermodynamic stabilities are confirmed by the tolerance factor and negative formation energy. Moreover, by doping Ti ions into vacancy-ordered double perovskite A_2SnY_6 , the effect of Ti doping on the electronic and optical properties was investigated in detail. Then, according to the requirement of practical applications in photovoltaics, the optimal concentration of Ti ions and the most suitable halide element are determined to screen the right compositions. In addition, the mechanical, electronic and optical properties of the selected compositions are discussed, exhibiting the maximum optical absorption both in the visible and ultraviolet energy ranges; thus, the selected compositions can be considered as promising materials for application in solar photovoltaics. The results suggest a great potential of $A_2Sn_{1-x}Ti_xY_6$ (A = K, Rb, Cs; Y = Cl, Br, I) for further theoretical research as well as experimental research on the photovoltaic performance of stable and toxic-free perovskite solar cells.

Keywords: vacancy-ordered; double perovskite; density functional theory; toxic-free; solar photovoltaics



Citation: Chen, W.; Liu, G.; Dong, C.; Guan, X.; Gao, S.; Hao, J.; Chen, C.; Lu, P. Investigation of Vacancy-Ordered Double Perovskite Halides $A_2Sn_{1-x}Ti_xY_6$ (A = K, Rb, Cs; Y = Cl, Br, I): Promising Materials for Photovoltaic Applications.

Nanomaterials **2023**, *13*, 2744.

<https://doi.org/10.3390/nano13202744>

Academic Editor: Elias Stathatos

Received: 2 September 2023

Revised: 26 September 2023

Accepted: 1 October 2023

Published: 11 October 2023



Copyright: © 2023 by the authors. Licensee MDPI, Basel, Switzerland. This article is an open access article distributed under the terms and conditions of the Creative Commons Attribution (CC BY) license (<https://creativecommons.org/licenses/by/4.0/>).

1. Introduction

The global energy demand keeps increasing owing to the development of the international economy, and this motivates researchers to seek alternatives to conventional fossil fuels, which are currently the main energy source but with limited reserves. Among the alternatives, solar energy is both clean and endless, but most importantly, it is conveniently available whenever and wherever possible. Therefore, it is considered as the long-term and economic substitute for fossil fuel. As the leading source of renewable energy, the performance of materials that are employed to use this energy source depends mostly on their band gap and feasibility of application. In this regard, considerable efforts have been made to find environmentally friendly and cost-effective technological systems and utilize the energy spectrum for solar cells and thermoelectric generators [1–4]. At present, the critical challenge is to find suitable materials, and much research has already been conducted to exploit their capability in energy conversion [5–7].

Hybrid organic–inorganic materials, methylammonium lead halides [8,9], in perovskite structures have proved successful as light absorbers in perovskite solar cells (PSCs) due to their unique optical and electronic properties, such as strong optical absorption, tunable band gap and large carrier diffusion length. The efficiency of single-junction PSCs were increased noticeably from 3.8% in 2009 [5] to 25.5% in 2022 [10,11], which exceeded that of

many conventional semiconductor absorbers. Moreover, Catchpole et al. reported an efficiency of 26.4% of solar cells by the tandem of PSCs and silicon-based solar cells [12], while the predicted theoretical photoelectric conversion efficiency (PCE) of PSCs is 31.4% [13]. Although hybrid organic–inorganic perovskite-based optoelectronic devices have been extensively researched, they are still far from commercialization since two critical problems still exist and are urgent to be overcome. One is the intrinsic toxicity of lead possibly leading to environmental pollution. The other is the poor structural stability of the volatile and hygroscopic organic cations to ambient environments, such as oxygen [14,15], humidity [16–18], light [19,20], temperature or thermal stress [21,22]. As a result, it is important to find all-inorganic lead-free perovskite materials for photovoltaics and other optoelectronic applications [23–26], and concerted efforts have been made to design new lead-free and stable halide perovskite for solar cells as well as other optoelectronic applications [27–29].

Among the suitable alternatives, the all-inorganic vacancy-ordered double perovskites of type A_2BX_6 have attracted much attention for application in photovoltaic technology due to their long-term stability and environmentally friendly properties [30,31]. They are a family of defect-ordered structural derivatives of the archetypal perovskite structure, and their structure is obtained by doubling the conventional perovskite ABX_3 unit cell along the three different crystallographic axes and then removing every other B-site cation. The remaining B-site cations form an ordered face-centered cubic arrangement. Since the $[BX_6]$ octahedrons are not connected by alternating B–X bonds, and each anion is coordinated to only one B-site cation, this structure can also be considered as an antifluorite arrangement of anionic isolated $[BX_6]$ octahedrons bridged by A-site cations, to which these materials are often referred. Compared with the conventional ABX_3 structure, the vacancy-ordered double perovskite A_2BX_6 structure has a tetravalent B-cation, instead of a bivalent B-cation in ABX_3 , which endows it with enhanced air and moisture stability under ambient conditions [23,30]. Although vacancy-ordered double perovskite materials have been studied in the literature, previous research almost exclusively focused on their structural and dynamic behaviors. Their properties relevant to specific potential applications in photovoltaics and other optoelectronics have been seldom studied systematically.

In order to further optimize the properties of materials, substitutional alloying or doping has been demonstrated to be a very effective strategy. Doping is at present an important method to improve the properties of perovskite materials, and vacancy-ordered double perovskite can be readily doped with different ions at all three sites to obtain the desired electronic and optical properties, especially in the sixfold coordinated tetravalent cation site. In addition, there are a large variety of tetravalent ions that may be introduced into the structure; thus, the compositional modification at the B-site of vacancy-ordered double perovskite A_2BX_6 may cause the largest flexibility in optical and electronic properties.

As the typical representation of vacancy-ordered double perovskite A_2SnY_6 , Cs_2SnI_6 was initially applied as a hole transport material for solar cells and attained ~8% efficiency [24]. After that, much attention has been paid to its research. Recent research on A_2SnY_6 has provided new prospects for a stabilized and environmentally friendly solar cell material [32,33]. Cs_2SnCl_6 , Cs_2SnBr_6 and Cs_2SnI_6 exhibit stable crystal structures at ambient temperature with a direct band gap semiconducting character and were found suitable for dye-sensitized solar cells [23]. However, there is still much room for improvement in the future; therefore, researchers are seeking different variants by compositional engineering to further enhance the power conversion efficiency of A_2SnY_6 perovskites.

In this work, we doped Ti ions into the B-site of a vacancy-ordered A_2SnY_6 double perovskite structure, and then explored the structural, electronic and optical properties of all-inorganic vacancy-ordered double perovskites $A_2Sn_{1-x}Ti_xY_6$ ($A = K, Rb, Cs$; $Y = Cl, Br, I$) by density functional theory. The effect of Ti doping on the electronic and optical properties is investigated and the optimal concentration of Ti ions and the most suitable halide element are determined to screen the right compositions for practical applications in photovoltaics. The mechanical, electronic and optical properties of the selected compositions are discussed

in detail. Our results are expected to provide a theoretical basis for the development of stable and toxic-free perovskite solar cells.

2. Computational Methods

All the calculations in this work were performed using the Vienna ab initio simulation package (VASP). The projector-augmented wave (PAW) method was applied to describe the interactions between the core and valence electrons. The electronic exchange and correlation energy was evaluated by using the generalized gradient approximation (GGA) in the form of Perdew–Burke–Ernzerhof (PBE) functional. The cut-off energy of 550 eV was used. The convergence criterion was set to 10^{-5} eV in energy, and all atomic positions and crystal structures involved in this work were fully relaxed with the force convergence at 0.01 eV/Å. During the optimizing geometry and static energy calculations, the Monkhorst–Pack k-point was chosen as $4 \times 4 \times 4$. The elastic constants C_{ij} were calculated by the strain–stress relationship with finite differences implemented in the VASP code.

3. Results and Discussions

3.1. Structural Properties of $A_2Sn_{1-x}Ti_xY_6$ ($A = K, Rb, Cs; Y = Cl, Br, I$)

The structural and thermodynamic stabilities of $A_2Sn_{1-x}Ti_xY_6$ ($A = K, Rb, Cs; Y = Cl, Br, I$) are necessary for energy devices. Doping concentrations of Ti^{4+} by face-center substitution with $x = 0, 0.25, 0.5, 0.75$ and 1 were considered in order to investigate the effect of Ti^{4+} doping. The optimized crystal parameters of $A_2Sn_{1-x}Ti_xY_6$ ($A = K, Rb, Cs; Y = Cl, Br, I$) are listed in Table S1 and the optimized crystal structures are plotted in Figure 1. According to Table S1, the lattice parameter and cell volume increase gradually with the increase in the atomic radius of A-site for the same B-site cation and Y-site anion. For the same A-site and B-site cations, the lattice parameter and cell volume increase gradually with the increase in the atomic radius of Y-site. When the A-site cation and Y-site anion are fixed, the lattice parameter and cell volume decrease monotonously with the increase in the concentration of Ti^{4+} , which indicates the contraction of the cell. Among all $A_2Sn_{1-x}Ti_xY_6$ perovskites, K_2TiCl_6 has the lowest lattice parameter, at 10.025 Å, and Cs_2SnI_6 has the highest lattice parameter, at 12.056 Å, which is very close to the reported values of 9.79 and 12.04 Å, respectively [34,35].

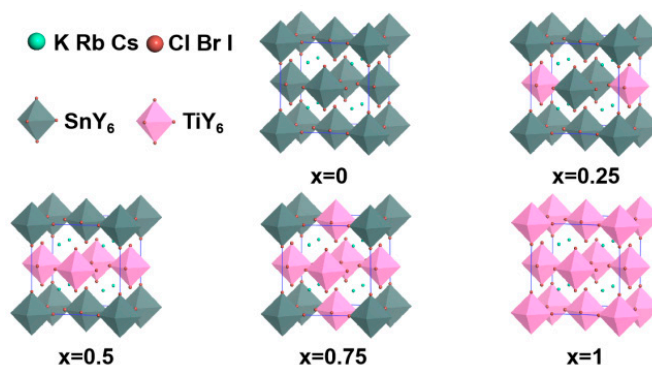


Figure 1. Optimized crystal structures of $A_2Sn_{1-x}Ti_xY_6$ ($A = K, Rb, Cs; Y = Cl, Br, I$).

The Goldschmidt tolerance factor t is used to evaluate whether the cation can be replaced in a perovskite material and predict the structural stability of perovskite materials, which is expressed by the following equation:

$$t = \frac{r_A + r_Y}{\sqrt{2}(r_{Sn/Ti} + r_Y)} \quad (1)$$

where r_A and r_Y are the Shannon's radii of A and Y atoms, respectively, and

$$r_{Sn/Ti} = (1 - x)r_{Sn} + xr_{Ti} \quad (2)$$

When the Goldschmidt's tolerance factor is in the range of 0.8–1.1, the structure of the materials is generally formed [36,37]. Our calculated results of the tolerance factor are shown in Figure 2, and it can be observed that the tolerance factor of $A_2Sn_{1-x}Ti_xY_6$ increases monotonously with the Ti content when the A-site cation and Y-site anion are fixed. When the Ti content and the A-site are fixed, the tolerance factor increases with the decrease in the atomic radius of the Y-site anion. When the Ti content and the Y-site are fixed, the tolerance factor increases with the increase in the atomic radius of the A-site cation. However, the tolerance factor is in the range of 0.96–1.08 for all $A_2Sn_{1-x}Ti_xY_6$ perovskites, which ensures their structural stability.

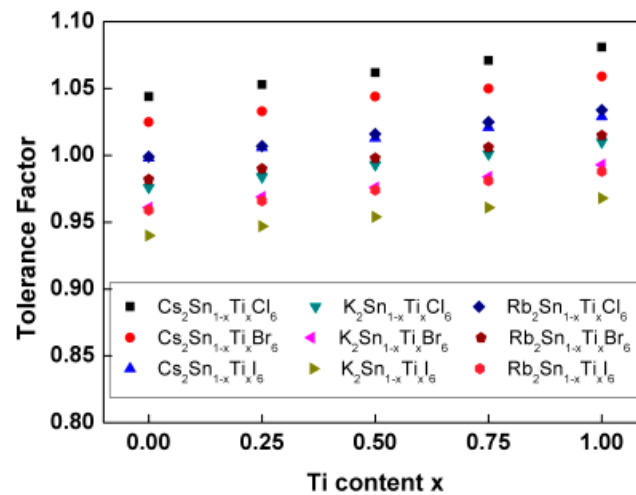


Figure 2. Tolerance factor of $A_2Sn_{1-x}Ti_xY_6$ ($A = K, Rb, Cs$; $Y = Cl, Br, I$).

In addition, in order to further study the thermodynamic stability of $A_2Sn_{1-x}Ti_xY_6$ perovskite materials, the formation energies E_f are obtained by the following formula [36]:

$$E_f = [E_{A_2Sn_{1-x}Ti_xY_6} - 2E_A - (1-x)E_{Sn} - xE_{Ti} - 6E_Y]/36 \quad (3)$$

where $E_{A_2Sn_{1-x}Ti_xY_6}$ is the total energy of the primitive cell; and E_A , E_{Sn} , E_{Ti} and E_Y are the energies of the A, Sn, Ti and Y atoms, respectively. According to Table 1, the formation energy decreases gradually in the order of $K > Rb > Cs$ for the same B-site cation and Y-site anion. For the same A-site and B-site cations, the formation energy increases gradually in the order of $Cl < Br < I$. When the A-site cation and Y-site anion are fixed, the formation energy decreases monotonously with the increase in the concentration of Ti^{4+} . All $A_2Sn_{1-x}Ti_xY_6$ perovskites exhibit negative values of formation energies, confirming that they are thermodynamically favorable, where Cs_2TiCl_6 has the lowest formation energy of -3.70 eV and K_2SnI_6 has the maximum formation energy of -2.19 eV.

Table 1. The formation energy of $A_2Sn_{1-x}Ti_xY_6$ ($A = K, Rb, Cs$; $Y = Cl, Br, I$).

| x | 0 | 0.25 | 0.5 | 0.75 | 1 |
|----------------------|-------|-------|-------|-------|-------|
| $KSn_{1-x}Ti_xCl_6$ | -2.99 | -3.16 | -3.34 | -3.51 | -3.68 |
| $KSn_{1-x}Ti_xBr_6$ | -2.61 | -2.77 | -2.93 | -3.09 | -3.26 |
| $KSn_{1-x}Ti_xI_6$ | -2.19 | -2.34 | -2.49 | -2.64 | -2.79 |
| $RbSn_{1-x}Ti_xCl_6$ | -3.00 | -3.17 | -3.34 | -3.51 | -3.69 |
| $RbSn_{1-x}Ti_xBr_6$ | -2.62 | -2.78 | -2.94 | -3.10 | -3.26 |
| $RbSn_{1-x}Ti_xI_6$ | -2.20 | -2.35 | -2.50 | -2.65 | -2.80 |
| $CsSn_{1-x}Ti_xCl_6$ | -3.01 | -3.19 | -3.36 | -3.53 | -3.70 |
| $CsSn_{1-x}Ti_xBr_6$ | -2.64 | -2.80 | -2.96 | -3.12 | -3.29 |
| $CsSn_{1-x}Ti_xI_6$ | -2.24 | -2.39 | -2.53 | -2.68 | -2.83 |

3.2. Screening of $A_2Sn_{1-x}Ti_xY_6$ ($A = K, Rb, Cs$; $Y = Cl, Br, I$) for Photovoltaic Applications

The band gap is an intrinsic property of materials that can not only influence the performance of the materials directly, but also provides information about the possible maximum theoretical efficiency of the materials. Thus, a critical factor for evaluating the performance of solar cells is the electronic band gap of the light absorber. The ideal band gap should be in the range of 0.9–1.6 eV [38] to obtain a theoretical efficiency higher than 25%. Especially when the band gap is around 1.3 eV, a maximum PCE in a single-junction solar cell can be achieved according to the Shockley–Queisser limit [39]. The electronic band structures of $A_2Sn_{1-x}Ti_xY_6$ ($A = K, Rb, Cs$; $Y = Cl, Br, I$) were calculated, and the compounds all displayed semiconductor characteristic. The band structures are shown in Figures S1–S3; Figure S1 shows the band structures of $K_2Sn_{1-x}Ti_xY_6$, Figure S2 shows the band structures of $Rb_2Sn_{1-x}Ti_xY_6$ and Figure S3 shows the band structures of $Cs_2Sn_{1-x}Ti_xY_6$. Figure 3a–c show the variation in band gap with the content of Ti in $A_2Sn_{1-x}Ti_xY_6$ ($A = K, Rb, Cs$; $Y = Cl, Br, I$). The band gap decreases gradually in the order of $Cl > Br > I$ for the same A-site and B-site cations, which is in agreement with the trend of band gap in $MAPbX_3$ ($X = Cl, Br, I$) halide perovskites [40]. With the increase in the A-site cation radius, the band gap also increases for the same B-site cation and Y-site anion, indicating that the tilting of the BY_6 ($B = Sn, Ti$) octahedron dictated by the A-site cation can influence the electronic structures of the material. Note that, when the Y-site is a Cl atom, the band gaps all decrease monotonically with the increase in Ti content. When the Y-site is a Br atom, the band gaps increase firstly and reach their maximum value at $x = 0.5$ before decreasing a little. When the Y-site is an I atom, the band gaps increase monotonically with the increase in Ti content. Based on the above calculation results, it can be observed that Ti doping plays a role in adjusting the band gap of $A_2Sn_{1-x}Ti_xY_6$ ($A = K, Rb, Cs$; $Y = Cl, Br, I$). In addition, we found that the band gaps of $A_2Sn_{1-x}Ti_xBr_6$ ($A = K, Rb, Cs$) are all in the range of 1.2–1.6 eV and are very close to that of $MAPbI_3$ [41–43], according to which the most suitable candidate for the Y-site is Br; thus, $A_2Sn_{1-x}Ti_xBr_6$ ($A = K, Rb, Cs$) can be considered as a promising material for photovoltaic applications.

Since the most significant role of lead-free halide double perovskite in solar cells and various opto-electronic applications is to act as a light-absorbing material, our primary focus was to find out its application in the visible and ultraviolet light absorption spectrum. The optical absorption is considered as an important property that can determine whether the material is suitable for photovoltaic applications. The absorption coefficient shows the light energy absorbed by the material, demonstrating direct transitions from the valence band maximum (VBM) to the conduction band minimum (CBM) owing to the absorption of the appropriate incident photon energies. For the sake of obtaining the optimal Ti doping concentration, Figure 3d–f show the optical adsorption spectra of $A_2Sn_{1-x}Ti_xBr_6$ ($A = K, Rb, Cs$) in a photon energy range from 0 to 4.5 eV. According to Figure 3d–f, the main optical absorption occurs in two energy ranges of 1.5–3.1 eV and 3.1–4.5 eV, which are mainly in the visible region and ultraviolet region, respectively. In both ranges, the replacement of the A-site cation shows a slight influence on the optical absorption, while the optical absorption intensity of $A_2Sn_{1-x}Ti_xBr_6$ ($A = K, Rb, Cs$) seems to be obviously influenced by the presence of the Ti dopant. With the increase in Ti content, the optical absorption coefficient increases monotonously, and when the Ti content $x = 1$, the optical absorption coefficient reaches a maximum value.

Moreover, in the range of 1.5–3.1 eV, the maximum optical absorption coefficient reaches 2.7×10^5 , 2.7×10^5 and 2.9×10^5 cm^{-1} for $A = K, Rb$ and Cs , respectively, indicating a strong optical absorption ability in the visible light region. In the range of 3.1–4.5 eV, the Ti dopant results in a significant absorption peak in the ultraviolet region. When the Ti content is $x = 0.25$, the peak value is approximately the same as that in the visible region. However, the peak value is even larger than that in the visible region with the further increase in Ti content x , and the peak position shifts to the higher energy direction. The maximum optical absorption coefficients of $A_2Sn_{1-x}Ti_xBr_6$ ($A = K, Rb, Cs$) are as high as 4.9×10^5 , 4.8×10^5 and 4.7×10^5 cm^{-1} for $A = K, Rb$ and Cs , respectively, indicating

their significant potential to be used in ultraviolet-light-based devices. These favorable absorption properties render A_2TiBr_6 ($A = K, Rb, Cs$) the most promising candidates for photovoltaic applications. Therefore, we only focused on the properties of A_2TiBr_6 ($A = K, Rb, Cs$) hereafter in this work.

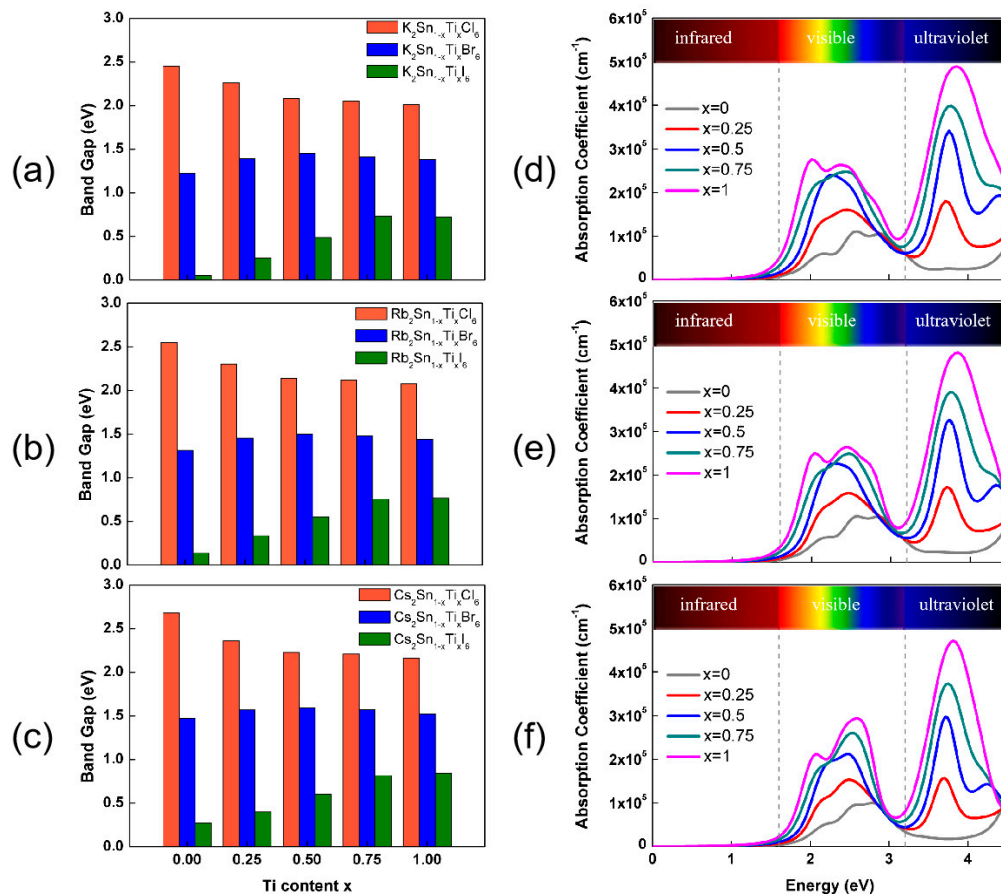


Figure 3. Band gaps of $A_2Sn_{1-x}Ti_xY_6$ ($A = K, Rb, Cs$; $Y = Cl, Br, I$) versus Ti content x : (a) $K_2Sn_{1-x}Ti_xY_6$, (b) $Rb_2Sn_{1-x}Ti_xY_6$ and (c) $Cs_2Sn_{1-x}Ti_xY_6$. Optical absorption spectra of $A_2Sn_{1-x}Ti_xBr_6$: $A = K$ in (d), $A = Rb$ in (e) and $A = Cs$ in (f).

3.3. Mechanical, Electronic and Optical Properties of A_2TiBr_6 ($A = K, Rb, Cs$)

In order to assess the mechanical stability of the materials, it is necessary to determine the elastic constants under applied stress. The elastic constants C_{ij} of A_2TiBr_6 ($A = K, Rb, Cs$) were calculated by the strain–stress relationship with finite differences implemented in the VASP code. Three independent elastic constants C_{11} , C_{12} and C_{44} were obtained for each compound of cubic A_2TiBr_6 ($A = K, Rb, Cs$). According to Born stability conditions, all the structures of A_2TiBr_6 ($A = K, Rb, Cs$) are mechanically stable. Other mechanical constants, such as the bulk modulus, shear modulus, Young’s modulus and Poisson’s ratio, were also calculated to investigate the mechanical behavior of A_2TiBr_6 ($A = K, Rb, Cs$) by the Voigt–Reuss–Hill (VRH) approximation for polycrystals with C_{ij} . Figure 4 shows the three-dimensional Young’s modulus and Poisson’s ratio of A_2TiBr_6 ($A = K, Rb, Cs$). Both the Young’s modulus and Poisson’s ratio decrease with the increase in the A-site ionic radius.

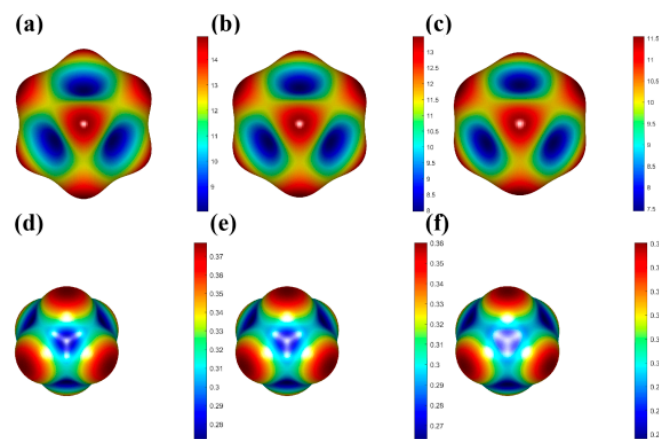


Figure 4. Three-dimensional Young's modulus of (a) K_2TiBr_6 , (b) Rb_2TiBr_6 and (c) Cs_2TiBr_6 and Poisson's ratio of (d) K_2TiBr_6 , (e) Rb_2TiBr_6 and (f) Cs_2TiBr_6 .

Figure 5 shows the mechanical properties of A_2TiBr_6 ($A = K, Rb, Cs$). It can be found that the elastic constants C_{11} , C_{12} and C_{44} decrease monotonously with the increase in the ionic radius of the A-site. K_2TiBr_6 has the highest C_{ij} and Cs_2TiBr_6 has the lowest C_{ij} . The increase in the ionic radius of the A site plays a more important role in decreasing the bulk modulus B and Young's modulus E than in decreasing the shear modulus G. The Pugh's ratio B/G and Poisson's ratio are two indicators that are usually used to evaluate the ductile or brittle behavior of solid materials. If the Pugh's ratio is lower than 1.75, the material is considered to be brittle; otherwise, it is ductile. For the Poisson's ratio, if its value is higher than 0.26, the material is considered to be ductile; otherwise, it is brittle. From Figure 5, it can be seen that the A_2TiBr_6 ($A = K, Rb, Cs$) perovskites are all ductile materials; thus, they are candidates of flexible photovoltaic devices. Since lower Pugh's ratio and Poisson's ratio values mean a higher hardness and vice versa, the hardness of A_2TiBr_6 ($A = K, Rb, Cs$) is in the order of $K_2TiBr_6 < Rb_2TiBr_6 < Cs_2TiBr_6$.

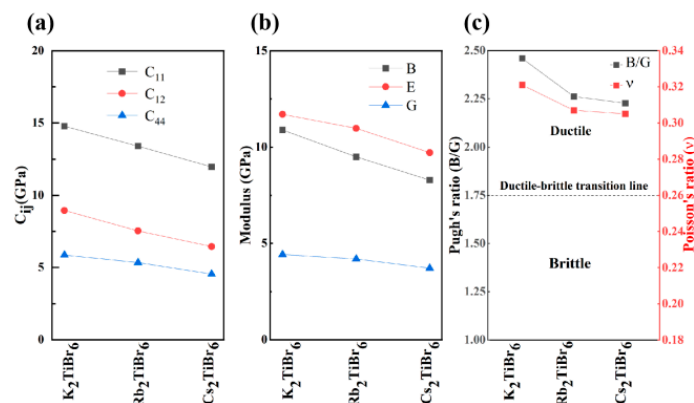


Figure 5. Mechanical properties of (a) K_2TiBr_6 , (b) Rb_2TiBr_6 and (c) Cs_2TiBr_6 .

Figure 6 shows the band structures and the density of states of A_2TiBr_6 ($A = K, Rb, Cs$). It can be observed that the band gap slightly increases with the increase in the A-site cation radius, which is 1.38, 1.43 and 1.52 eV, for K_2TiBr_6 , Rb_2TiBr_6 and Cs_2TiBr_6 , respectively. In order to better understand the origin of the conduction band and valence band, the density of states (DOS) and partial DOS of A_2TiBr_6 ($A = K, Rb, Cs$) were plotted. It can be seen that the Br-4p orbitals mainly contribute to the VBM, while the CBM receives its primary contribution from the Ti-3d orbital and a very small amount from the Br-4p orbital. The A-site cations in A_2TiBr_6 ($A = K, Rb, Cs$) contribute little to the band edges, indicating no direct influence on the band gaps.

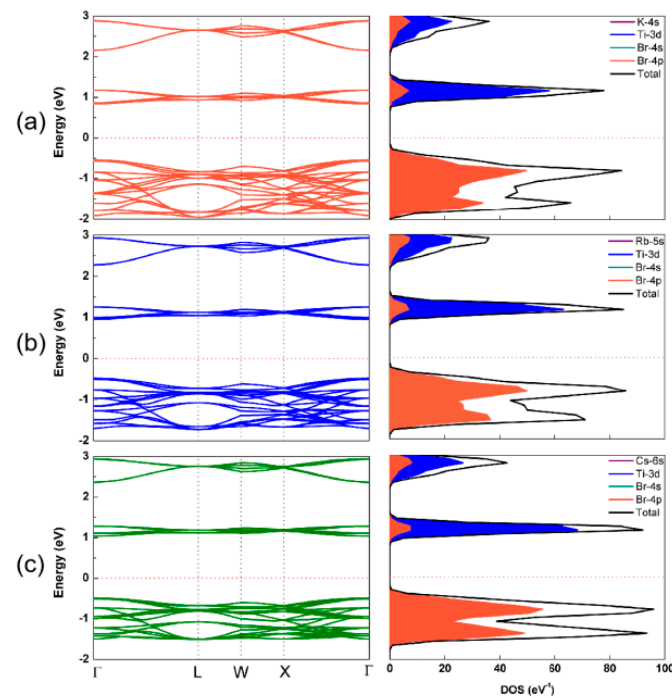


Figure 6. Band structures and density of states of (a) K_2TiBr_6 , (b) Rb_2TiBr_6 and (c) Cs_2TiBr_6 .

In order to further check the orbital contribution, the decomposed charge density distribution of VBM and CBM were calculated and are plotted in Figure 7. It can be seen that the charge density of VBM is distributed on all Br atoms composed of antibonding state of Br-4p and Br-4p, while the charge density of CBM is mainly distributed on Ti atoms. Both the partial DOS and the decomposed charge density confirm the negligible contribution of the A-site to the band edge and, as a result, there is no direct influence on the band gap.

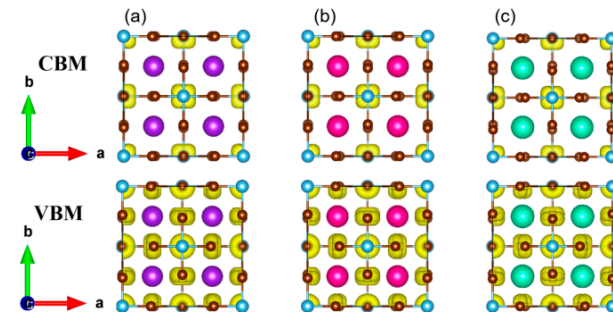


Figure 7. Charge density of CBM and VBM of (a) K_2TiBr_6 , (b) Rb_2TiBr_6 and (c) Cs_2TiBr_6 .

To confirm the possible application of A_2TiBr_6 ($A = K, Rb, Cs$) as a photovoltaic material, the various optical parameters of A_2TiBr_6 ($A = K, Rb, Cs$) were calculated for the incident energy range of 0–25 eV, as shown in Figure 8. The dielectric constant is the most important parameter to illustrate the optical behavior of the material and it can be used to calculate several parameters. The real part of the dielectric constant $\epsilon_1(\omega)$ shows the polarization and dispersion of impinging light, and the static dielectric constant $\epsilon_1(0)$ is 3.67, 3.44 and 3.17 for K_2TiBr_6 , Rb_2TiBr_6 and Cs_2TiBr_6 , respectively, according to Figure 8a, which are inversely related to the respective band gaps. The imaginary part $\epsilon_2(\omega)$ demonstrates the light absorption with the maximum absorption peaks at around 1.9–2.0 eV for A_2TiBr_6 ($A = K, Rb, Cs$), as shown in Figure 8b. The absorption coefficient measures the ability of the materials to absorb light energy per centimeter. Figure 8c shows the absorption spectrum of A_2TiBr_6 ($A = K, Rb, Cs$), in which the absorption edges are very important to indicate the critical points after which the absorption linearly increases, and for A_2TiBr_6 ($A = K, Rb, Cs$),

the absorption edges are all in the infrared energy range. In the visible energy range (1.77–3.18 eV), the dominant absorption peak shifts to a higher energy direction when A is from K to Cs. The refractive index is the ratio of the speed of light in vacuum to the speed of light in the material, often used to measure the transparency of materials and it provides details similar to the real part of the dielectric constant; thus, both curves display similar trends. The calculated static refractive index $n(0)$ for A_2TiBr_6 ($A = K, Rb, Cs$) was 1.91, 1.85 and 1.78, respectively, as shown in Figure 8d. Since the calculated static dielectric constant is 3.67, 3.44 and 3.17, it is evident that these two parameters follow the following relation:

$$n(\omega) = \sqrt{\varepsilon_1(\omega)} \quad (4)$$

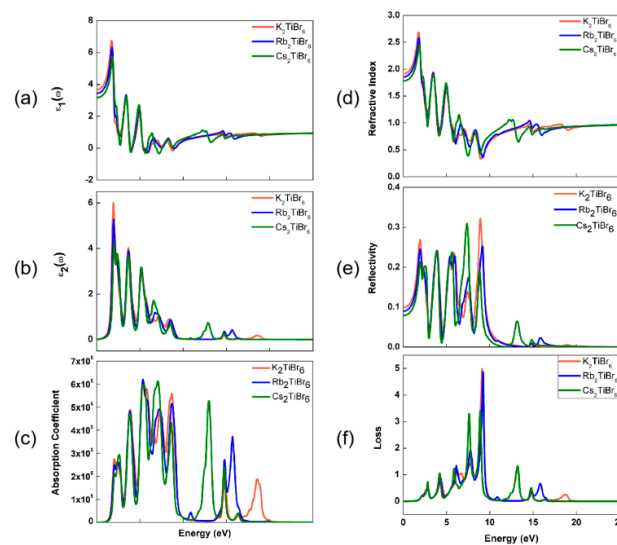


Figure 8. Calculated optical parameters of A_2TiBr_6 ($A = K, Rb, Cs$): (a) real dielectric constant, (b) imaginary dielectric constant, (c) absorption coefficient, (d) refractive index coefficient, (e) reflectivity coefficient and (f) loss coefficient.

The reflectivity shows the ability of the material to reflect the incident energies to its surface, and the static reflectivity $R(0)$ of A_2TiBr_6 ($A = K, Rb, Cs$) is 9.8, 9.0 and 7.9%, respectively, according to Figure 8e, which can be used to evaluate the surface quality. The maximum reflectivity is obtained as 31.9, 25.1 and 30.8% at 8.9, 9.2 and 7.4 eV, respectively. The loss factor $L(\omega)$ shows the energy loss due to the dispersion and scattering of light, usually representing the interband, intraband and plasmonic interactions, which is displayed in Figure 8f. The energy loss occurs when electrons move at a high speed through the material and scatter, and reaches its maximum value when the energy of the incident light is approximately 9 eV. Since the band gaps of A_2TiBr_6 ($A = K, Rb, Cs$) are well below the energies where electron energy losses are maximum, A_2TiBr_6 ($A = K, Rb, Cs$) are potential materials for photovoltaic applications.

4. Conclusions

In summary, we predicted a series of vacancy-ordered, lead-free, Ti-based all-inorganic double perovskites for photovoltaic applications by density functional theory. The comprehensive theoretical investigation of the structural stability, mechanical, electronic and optical properties of $A_2Sn_{1-x}Ti_xY_6$ ($A = K, Rb, Cs$; $Y = Cl, Br, I$) was performed. The calculated tolerance factors of $A_2Sn_{1-x}Ti_xY_6$ ($A = K, Rb, Cs$; $Y = Cl, Br, I$) are in the range of 0.96–1.08 for all compositions, which ensures their structural stability. The calculated negative formation energies confirm they are also thermodynamically favorable. The band structure and optical absorption results show that $A_2Sn_{1-x}Ti_xBr_6$ ($A = K, Rb, Cs$) compounds all show semiconductor characteristics with band gaps in the range of 0.9–1.6 eV, and A_2TiBr_6 ($A = K, Rb, Cs$) compounds have the maximum optical absorption both in the

visible and ultraviolet energy ranges; thus, they can be considered as promising materials for photovoltaic applications. For A_2TiBr_6 ($A = K, Rb, Cs$) compounds, they are all ductile perovskites with mechanically stable structures. The VBM of A_2TiBr_6 ($A = K, Rb, Cs$) receives its mainly contribution from the Br-4p orbitals and the charge density of VBM is distributed on all Br atoms composed of the antibonding state of Br-4p and Br-4p. The CBM of A_2TiBr_6 ($A = K, Rb, Cs$) receives its primary contribution from the Ti-3d orbital and a very small amount from the Br-4p orbital, and the charge density of CBM is mainly distributed on Ti atoms. This work can provide theoretical guidance for further theoretical research as well as experimental research on the application of A_2TiBr_6 ($A = K, Rb, Cs$) in photovoltaic and other optoelectronic applications.

Supplementary Materials: The following supporting information can be downloaded at: <https://www.mdpi.com/article/10.3390/nano13202744/s1>. Figure S1: Band structures of $K_2Sn_{1-x}Ti_xY_6$ all-inorganic double perovskites; Figure S2: Band structures of $Rb_2Sn_{1-x}Ti_xY_6$ all-inorganic double perovskites; Figure S3: Band structures of $Cs_2Sn_{1-x}Ti_xY_6$ all-inorganic double perovskites; Table S1: The optimized lattice parameters of A_2TiBr_6 ($A = K, Rb, Cs$) all-inorganic double perovskites.

Author Contributions: Conceptualization, W.C. and G.L.; methodology, C.D.; software, S.G.; validation, J.H.; formal analysis, C.C.; investigation, X.G.; resources and supervision, P.L. All authors have read and agreed to the published version of the manuscript.

Funding: National Key Research and Development Program of China (No.2021YFB3601201), the Natural Science Foundation of Shaanxi Province (No. 2023-JC-YB-065, 2021JM-371), the Open-Foundation of Key Laboratory of Laser Device Technology and the Fund of State Key Laboratory of IPOC (BUPT) (No. IPOC2019A013).

Data Availability Statement: Not applicable.

Acknowledgments: This work was supported by the National Key Research and Development Program of China (No.2021YFB3601201), the Natural Science Foundation of Shaanxi Province (No. 2023-JC-YB-065, 2021JM-371), the Open-Foundation of Key Laboratory of Laser Device Technology and the Fund of State Key Laboratory of IPOC (BUPT) (No. IPOC2019A013).

Conflicts of Interest: The authors declare no conflict of interest.

References

1. Abiram, G.; Gourji, F.H.; Pitchaiya, S.; Ravirajan, P.; Murugathas, T.; Velauthapillai, D. Air processed $Cs_2AgBiBr_6$ lead-free double perovskite high-mobility thin-film field-effect transistors. *Sci. Rep.* **2022**, *12*, 2455. [[CrossRef](#)]
2. Kumari, D.; Pandey, S.K. Comprehensive study and performance analysis of an eco-friendly double perovskite $Cs_2AgBiBr_6$ on Si tandem solar cell. *J. Opt. Soc. Am. B* **2022**, *39*, 756–763. [[CrossRef](#)]
3. Yu, F.; Liu, J.; Xu, P.; Huang, J.-H.; Li, C.-H.; Zheng, Y.-X. High-quality all-inorganic $CsPbI_2Br$ thin films derived from phase-pure intermediate for efficient wide-bandgap perovskite solar cells. *J. Solid State Chem.* **2023**, *317*, 123728. [[CrossRef](#)]
4. Kumar, J.; Hembram, K.P.S.S. Interface properties of $CsPbBr_3/CsPbI_3$ perovskite heterostructure for solar cell. *Phys. B* **2022**, *625*, 413472. [[CrossRef](#)]
5. Eperon, G.E.; Leijtens, T.; Bush, K.A.; Prasanna, R.; Green, T.; Wang, J.T.; Mcmeekin, D.P.; Volonakis, G.; Milot, R.L.; May, R.; et al. Perovskite-perovskite tandem photovoltaics with optimized band gaps. *Science* **2016**, *354*, 861–865. [[CrossRef](#)] [[PubMed](#)]
6. Montes, F.R.; Rosiles-Perez, C.; Ramos, C.F.A.; Hu, H.-L.; Sanchez, J.L.S.; Gonzalez, A.E.J. Study of DMSO concentration on the optical and structural properties of perovskite $CH_3NH_3PbI_3$ and its use in solar cells. *J. Solid State Chem.* **2022**, *312*, 123158. [[CrossRef](#)]
7. Yang, W.S.; Park, B.-W.; Jung, E.H.; Jeon, N.J.; Kim, Y.C.; Lee, D.U.; Shin, S.S.; Seo, J.; Kim, E.K.; Noh, J.H.; et al. Iodide management in formamidinium-lead-halide-based perovskite layers for efficient solar cells. *Science* **2017**, *356*, 1376–1379. [[CrossRef](#)]
8. Ahn, S.M.; Jung, E.D.; Kim, S.-H.; Kim, H.; Lee, S.; Song, M.H.; Kim, J.-Y. Nanomechanical Approach for Flexibility of Organic-Inorganic Hybrid Perovskite Solar Cells. *Nano Lett.* **2019**, *19*, 3707–3715. [[CrossRef](#)]
9. Lee, M.M.; Miyasaka, J.T.T.; Murakami, T.N.; Snaith, H.J. Efficient Hybrid Solar Cells Based on Meso-Superstructured Organometal Halide Perovskites. *Science* **2012**, *338*, 643–647. [[CrossRef](#)]
10. Best Research-Cell Efficiency Chart. 2020. Available online: <https://www.nrel.gov/pv/cell-efficiency.html> (accessed on 2 July 2022).
11. Green, M.A.; Dunlop, E.D.; Ebinger, J.H.; Yoshita, M.; Hao, N.K.X.-J. Solar cell efficiency tables (version 59). *Prog. Photovolt.* **2022**, *30*, 3–12. [[CrossRef](#)]

12. Catchpole, K.R. High efficiency perovskite/silicon tandems for electricity and hydrogen. In Proceedings of the 2021 IEEE 48th Photovoltaic Specialists Conference (PVSC), Fort Lauderdale, FL, USA, 20–25 June 2021; pp. 2279–2280.
13. Park, N.G.; Segawa, H. Research Direction toward Theoretical Efficiency in Perovskite Solar Cells. *ACS Photonics* **2018**, *5*, 2970–2977. [[CrossRef](#)]
14. Aristidou, N.; Eames, C.; Molina, I.S.; Bu, X.-N.; Kosco, J.; Islam, M.S.; Haque, S.A. Fast oxygen diffusion and iodide defects mediate oxygen-induced degradation of perovskite solar cells. *Nat. Commun.* **2017**, *8*, 15218. [[CrossRef](#)] [[PubMed](#)]
15. Senocrate, A.; Acarturk, T.; Kim, G.Y.; Merkle, R.; Starke, U.; Gratzel, M.; Maier, J. Interaction of oxygen with halide perovskites. *J. Mater. Chem. A* **2018**, *6*, 10847–10855. [[CrossRef](#)]
16. Salado, M.; Bernal, L.C.; Calio, L.; Todinova, A.; Santos, C.L.; Ahmad, S.; Borrás, A.; Idigoras, J.; Anta, J.A. Impact of moisture on efficiency-determining electronic processes in perovskite solar cells. *J. Mater. Chem. A* **2017**, *5*, 10917–10927. [[CrossRef](#)]
17. Yang, J.-L.; Siempelkamp, B.D.; Liu, D.-Y.; Kelly, T.L. Investigation of CH₃NH₃PbI₃ Degradation Rates and Mechanisms in Controlled Humidity Environments Using in Situ Techniques. *ACS Nano* **2015**, *9*, 1955–1963. [[CrossRef](#)] [[PubMed](#)]
18. Yun, J.S.; Kim, J.; Young, T.; Patterson, R.J.; Kim, D.; Seidel, J.; Lim, S.; Green, M.A.; Huang, S.-J.; Baillie, A.H. Humidity-Induced Degradation via Grain Boundaries of HC(NH₂)₂PbI₃ Planar Perovskite Solar Cells. *Adv. Funct. Mater.* **2018**, *28*, 1705363. [[CrossRef](#)]
19. Bastos, J.P.; Paetzold, U.W.; Gehlhaar, R.; Qiu, W.-M.; Cheyns, D.; Surana, S.; Spampinato, V.; Aernouts, T.; Poortmans, J. Light-Induced Degradation of Perovskite Solar Cells: The Influence of 4-Tert-Butyl Pyridine and Gold. *Adv. Energy Mater.* **2018**, *8*, 1800554. [[CrossRef](#)]
20. Li, Y.-Z.; Xu, X.-M.; Wang, C.-C.; Ecker, B.; Yang, J.-L.; Huang, J.-S.; Gao, Y.-L. Light-Induced Degradation of CH₃NH₃PbI₃ Hybrid Perovskite Thin Film. *J. Phys. Chem. C* **2017**, *121*, 3904–3910. [[CrossRef](#)]
21. Conings, B.; Drijkoningen, J.; Gauquelin, N.; Babayigit, A.; Haen, J.D.; Olieslaeger, L.D.; Ethirajan, A.; Verbeeck, J.; Manca, J.; Mosconi, E.; et al. Intrinsic Thermal Instability of Methylammonium Lead Trihalide Perovskite. *Adv. Energy Mater.* **2015**, *5*, 1500477. [[CrossRef](#)]
22. Juarez-Perez, E.J.; Ono, L.K.; Maeda, M.; Jiang, Y.; Hawash, Z.; Qi, Y.-B. Photodecomposition and thermal decomposition in methylammonium halide lead perovskites and inferred design principles to increase photovoltaic device stability. *J. Mater. Chem. A* **2018**, *6*, 9604–9612. [[CrossRef](#)]
23. Kaltzoglou, A.; Antoniadou, M.; Kontos, A.G.; Stoumpos, C.C.; Perganti, D.; Siranidi, E.; Raptis, V.; Trohidou, K.; Psycharis, V.; Kanatzidis, M.G.; et al. Optical-Vibrational Properties of the Cs₂SnX₆ (X = Cl, Br, I) Defect Perovskites and Hole-Transport Efficiency in Dye-Sensitized Solar Cells. *J. Phys. Chem. C* **2016**, *120*, 11777–11785. [[CrossRef](#)]
24. Lee, B.; Stoumpos, C.C.; Zhou, N.-J.; Hao, F.; Malliakas, C.; Yeh, C.-Y.; Marks, T.J.; Kanatzidis, M.G.; Chang, R.P.H. Air-Stable Molecular Semiconducting Iodosalts for Solar Cell Applications: Cs₂SnI₆ as a Hole Conductor. *J. Am. Chem. Soc.* **2014**, *136*, 15379–15385. [[CrossRef](#)] [[PubMed](#)]
25. Maughan, A.E.; Ganose, A.M.; Bordelon, M.M.; Miller, E.M.; Scanlon, D.O.; Neilson, J.R. Defect Tolerance to Intolerance in the Vacancy-Ordered Double Perovskite Semiconductors Cs₂SnI₆ and Cs₂TeI₆. *J. Am. Chem. Soc.* **2016**, *138*, 8453–8464. [[CrossRef](#)]
26. Saparov, B.; Hong, F.; Sun, J.-P.; Duan, H.-S.; Meng, W.-W.; Cameron, S.; Hill, I.G.; Yan, Y.-F.; Mitzi, D.B. Thin-Film Preparation and Characterization of Cs₃Sb₂I₉: A Lead-Free Layered Perovskite Semiconductor. *Chem. Mater.* **2015**, *27*, 5622–5632. [[CrossRef](#)]
27. Hao, F.; Stoumpos, C.C.; Chang, R.P.H.; Kanatzidis, M.G. Anomalous Band Gap Behavior in Mixed Sn and Pb Perovskites Enables Broadening of Absorption Spectrum in Solar Cells. *J. Am. Chem. Soc.* **2014**, *136*, 8094–8099. [[CrossRef](#)]
28. Krishnamoorthy, T.; Ding, H.; Yan, C.; Leong, W.-L.; Baikie, T.; Zhang, Z.-Y.; Sherburne, M.; Li, S.-Z.; Aska, M.; Mathews, N.; et al. Lead-free germanium iodide perovskite materials for photovoltaic applications. *J. Mater. Chem. A* **2015**, *3*, 23829–23832. [[CrossRef](#)]
29. Liang, L.S.; Gao, P. Lead-Free Hybrid Perovskite Absorbers for Viable Application: Can We Eat the Cake and Have It too? *Adv. Sci.* **2018**, *5*, 1700331. [[CrossRef](#)]
30. Saparov, B.; Sun, J.-P.; Meng, W.-W.; Xiao, Z.-W.; Duan, H.-S.; Gunawan, O.; Shin, D.; Hill, I.G.; Yan, Y.-F.; Mitzi, D.B. Thin-Film Deposition and Characterization of a Sn-Deficient Perovskite Derivative Cs₂SnI₆. *Chem. Mater.* **2016**, *28*, 2315–2322. [[CrossRef](#)]
31. Faizan, M.; Wang, X.-J.; Abdelmohsen, S.A.M.; Bhamu, K.C.; Sappati, S.; Laref, A.; Muhammad, N.; Mushtaq, M.; Abdelbacki, A.M.M.; Khenata, R. Understanding the electronic structure and optical properties of vacancy-ordered double perovskite A₂BX₆ for optoelectronic applications. *Energy Fuels* **2022**, *36*, 7065–7074. [[CrossRef](#)]
32. Faizan, M.; Xie, J.; Murtaza, G.; Echeverría-Arrondo, C.; Alshahrani, T.; Bhamu, K.C.; Laref, A.; Mora-Seró, I.; Khan, S.H. A first-principles study of the stability, electronic structure, and optical properties of halide double perovskite Rb₂Sn_{1-x}Te_xI₆ for solar cell applications. *Phys. Chem. Chem. Phys.* **2021**, *23*, 4646–4657. [[CrossRef](#)]
33. Faizan, M.; Khan, S.H.; Khachai, H.; Seddik, T.; Omran, S.B.; Khenata, R.; Xie, J.; AL-Anazy, M.M. Electronic, optical, and thermoelectric properties of perovskite variants A₂BX₆: Insight and design via first-principles calculations. *Int. J. Energy Res.* **2021**, *45*, 4495–4507. [[CrossRef](#)]
34. Bland, J.A.; Flengas, S.N. The crystal structure of F K₂TiCl₆. *Can. J. Phys.* **1961**, *39*, 941–944. [[CrossRef](#)]
35. Ma, X.X.; Li, Z.S. Influence of Sn/Ge Cation Exchange on Vacancy-Ordered Double Perovskite Cs₂Sn_(1-x)Ge_xI₆: A First-Principles Theoretical Study. *Phys. Status Solidi (B)* **2019**, *256*, 1800427. [[CrossRef](#)]
36. Li, C.; Lu, X.; Ding, W.; Feng, L.; Gao, Y.; Guo, Z. Formability of ABX₃ (X = F, Cl, Br, I) halide perovskites. *Acta Crystallogr. Sect. B-Struct. Sci. Cryst. Eng. Mater.* **2008**, *64*, 702–707. [[CrossRef](#)]

37. Manser, J.S.; Christians, J.A.; Kamat, P.V. Intriguing Optoelectronic Properties of Metal Halide Perovskites. *Chem. Rev.* **2016**, *116*, 12956–13008. [[CrossRef](#)]
38. Loferski, J.J. Theoretical Considerations Governing the Choice of the Optimum Semiconductor for Photovoltaic Solar Energy Conversion. *J. Appl. Phys.* **1956**, *27*, 777–784. [[CrossRef](#)]
39. Shockley, W.; Queisser, H.J. Detailed Balance Limit of Efficiency of P-N Junction Solar Cells. *J. Appl. Phys.* **1961**, *32*, 510. [[CrossRef](#)]
40. Ju, M.G.; Dai, J.; Ma, L.; Zeng, X.-C. Perovskite Chalcogenides with Optimal Bandgap and Desired Optical Absorption for Photovoltaic Devices. *Adv. Energy Mater.* **2017**, *7*, 1700216. [[CrossRef](#)]
41. Liu, S.; Zheng, F.; Koocher, N.Z.; Takenaka, H.; Wang, F.-G.; Rappe, A.M. Ferroelectric Domain Wall Induced Band Gap Reduction and Charge Separation in Organometal Halide Perovskites. *J. Phys. Chem. Lett.* **2015**, *6*, 693–699. [[CrossRef](#)]
42. Mosconi, E.; Umari, P.; De Angelis, F. Electronic and optical properties of mixed Sn-Pb organohalide perovskites: A first principles investigation. *J. Mater. Chem. A* **2015**, *3*, 9208–9215. [[CrossRef](#)]
43. Ogomi, Y.; Morita, A.; Tsukamoto, S.; Saitho, T.; Fujikawa, N.; Shen, Q.; Toyoda, T.; Pandey, K.Y.S.S.; Ma, T.; Hayase, S. $\text{CH}_3\text{NH}_3\text{Sn}_x\text{Pb}_{(1-x)}\text{I}_3$ Perovskite Solar Cells Covering up to 1060 nm. *J. Phys. Chem. Lett.* **2014**, *5*, 1004–1011. [[CrossRef](#)] [[PubMed](#)]

Disclaimer/Publisher’s Note: The statements, opinions and data contained in all publications are solely those of the individual author(s) and contributor(s) and not of MDPI and/or the editor(s). MDPI and/or the editor(s) disclaim responsibility for any injury to people or property resulting from any ideas, methods, instructions or products referred to in the content.